Coexistence of polar displacements and conduction in doped ferroelectrics: An *ab initio* comparative study

Chengliang Xia,[1,2] Yue Chen,[1,*] and Hanghui Chen[2,3,†]
[1]*Department of Mechanical Engineering, The University of Hong Kong, Pokfulam Road, Hong Kong SAR, China*
[2]*NYU-ECNU Institute of Physics, NYU Shanghai, Shanghai 200062, China*
[3]*Department of Physics, New York University, New York, New York 10003, USA*

(Received 9 December 2018; published 15 May 2019)

Polar metals are rare because free carriers in metals screen electrostatic potential and eliminate internal dipoles. Degenerate doped ferroelectrics may create an approximate polar metallic phase. We use first-principles calculations to investigate *n*-doped $LiNbO_3$-type oxides ($LiNbO_3$ as the prototype) and compare to widely studied perovskite oxides ($BaTiO_3$ as the prototype). In the rigid-band approximation, substantial polar displacements in *n*-doped $LiNbO_3$ persist even at 0.3 e/f.u. ($\simeq 10^{21}$ cm^{-3}), while polar displacements in *n*-doped $BaTiO_3$ quickly get suppressed and completely vanish at 0.1 e/f.u. Furthermore, in *n*-doped $LiNbO_3$, Li-O displacements decay more slowly than Nb-O displacements, while in *n*-doped $BaTiO_3$, Ba-O and Ti-O displacements decay approximately at the same rate. Supercell calculations that use oxygen vacancies as electron donors support the main results from the rigid-band approximation and provide more detailed charge distributions. Substantial cation displacements are observed throughout $LiNbO_{3-\delta}$ ($\delta = 4.2\%$), while cation displacements in $BaTiO_{3-\delta}$ ($\delta = 4.2\%$) are almost completely suppressed. We find that conduction electrons in $LiNbO_{3-\delta}$ are not as uniformly distributed as in $BaTiO_{3-\delta}$, implying that the rigid-band approximation should be used with caution in simulating electron-doped $LiNbO_3$-type oxides. Our work shows that polar distortions and conduction can coexist in a wide range of electron concentration in *n*-doped $LiNbO_3$, which is a practical approach to generating an approximate polar metallic phase. Combining doped ferroelectrics and doped semiconductors may create new functions for devices.

DOI: 10.1103/PhysRevMaterials.3.054405

I. INTRODUCTION

Polar metals are materials that are characterized by the absence of inversion symmetry and the presence of intrinsic conduction due to partial band occupation [1–5]. They are rare in solids because free carriers can screen electrostatic potential and eliminate internal dipoles that arise from asymmetric charge distributions [6–10]. Anderson and Blount predicted in 1965 that polar metals can exist [11], and the recent experimental confirmation of $LiOsO_3$ as the first polar metal has stimulated intensive theoretical and experimental research [12–21].

However, the above definition of a polar metal (absence of inversion symmetry and presence of conduction) excludes degenerately doped insulating ferroelectrics [21]. Electron-doped perovskite ferroelectric compounds ABO_3 ($BaTiO_3$ as the prototype) have been widely studied both in theory and in experiment [22–28]. First-principles calculations show that cation displacements and conduction can coexist in *n*-doped $BaTiO_3$ up to a critical concentration of $0.1e$ per formula [26]. This indicates that even with long-range Coulomb interaction screened by free electrons [29–31], a short-range portion of Coulomb force with an interaction range of the order of the lattice constant is sufficient to induce ferroelectric instability in $BaTiO_3$ [26,32,33]. Experimentally, there are contradictory results: Refs. [23,24] show that in oxygen-reduced $BaTiO_{3-\delta}$, polar displacements can coexist with conduction and do not vanish until a critical concentration of 1.9×10^{21}cm^{-3}, which is consistent with first-principles calculations [26]. However, a neutron diffraction study on *n*-doped $BaTiO_3$ found phase separation in which ferroelectric displacements only exist in an insulating region, which is spatially separated by nonpolar metallic regions [22]. On the other hand, while electron-doped $LiNbO_3$-type ferroelectric oxides ($LiNbO_3$ as the prototype) have been investigated in the literature, the focus has been on electronic structure and the optical property [34–37]. The structural property and the possible coexistence of polar displacements with conduction have received little attention.

In this work, we use first-principles calculations to do a comparative study on doping effects in insulating ferroelectrics. We compare the aforementioned two important classes of ferroelectrics: one is perovskite oxides ($BaTiO_3$ as the prototype) and the other is $LiNbO_3$-type oxides ($LiNbO_3$ as the prototype). We find different behaviors in these two materials upon electron doping. In the rigid-band approximation, cation displacements in *n*-doped $BaTiO_3$ quickly get suppressed and completely disappear at a critical doping of 0.1 e/f.u., while substantial cation displacements are found in *n*-doped $LiNbO_3$ up to an electron concentration of 0.3 e/f.u.. Moreover, Li-O displacements decay more slowly than Nb-O displacements. With an electron doping of 0.3 e/f.u., Nb-O displacements are reduced by about 50% from the undoped

*yuechen@hku.hk
†hanghui.chen@nyu.edu

value, while Li-O displacements are reduced by only about 10%. This is different from n-doped $BaTiO_3$, in which both Ba-O and Ti-O displacements decay approximately at the same rate. This indicates that Li-O displacements are more persistent than Nb-O displacements in a metallic environment. Supercell calculations that use oxygen vacancy as electron donors support the main results from the rigid-band approximation and provide more detailed charge distributions. We find that in n-doped $LiNbO_3$, conduction electrons are not as uniformly distributed as in n-doped $BaTiO_3$, but substantial cation displacements are found throughout n-doped $LiNbO_3$. Using supercell calculations, we also compute the formation energy of oxygen vacancies. The formation energy of oxygen vacancies in n-doped $LiNbO_3$ is about 1 eV higher than that in n-doped $BaTiO_3$, which is reasonable considering the fact that the band gap of $LiNbO_3$ is about 1 eV larger than that of $BaTiO_3$.

The paper is organized as follows. In Sec. II we provide computation details. We present the main results (rigid-band calculations and supercell calculations) in Sec. III. We conclude in Sec. IV.

II. COMPUTATIONAL DETAILS

We perform density functional (DFT) calculations [38,39], as implemented in the Vienna Ab-initio Simulation Package (VASP) [40,41]. We employ a local density approximation (LDA) pseudopotential [42]. We also test our key results using a revised Perdew-Burke-Ernzerhof generalized gradient approximation (PBEsol) [43]. The key results do not qualitatively change with different exchange correlation functionals. We set an energy cutoff of 600 eV. Charge self-consistent calculations are converged to 10^{-5} eV. Both cell and internal coordinates are fully relaxed until each force component is smaller than 10 meV/Å and the stress tensor is smaller than 1 kbar.

For pristine bulk calculations, we use a tetragonal cell (5-atom) to study $BaTiO_3$ and find that $a = 3.95$ Å and $c/a = 1.01$; we use a hexagonal cell (30-atom) to study $R3c$ $LiNbO_3$ and find that $a = 5.09$ Å and $c = 13.81$ Å. Both of them are in good agreement with previous studies [44].

To simulate doping effects, we use both the rigid-band approximation and supercell calculations. In rigid-band modeling, we study a 5-atom cell $BaTiO_3$ (tetragonal $P4mm$ and cubic $Pm\bar{3}m$) and a 30-atom cell $LiNbO_3$ (noncentrosymmetric $R3c$ and centrosymmetric $R\bar{3}c$). We use a Monkhorst-Pack k-point sampling of $14 \times 14 \times 14$ for $BaTiO_3$ and $8 \times 8 \times 3$ for $LiNbO_3$. In supercell calculations, we use a 119-atom cell for both $BaTiO_3$ and $LiNbO_3$ (oxygen-vacancy concentration of 4.2%/f.u. and nominal electron doping of 0.084 e/f.u.). The supercells for $BaTiO_3$ and $LiNbO_3$ are shown in Figs. 4 and 5. We use a Monkhorst-Pack k-point sampling of $8 \times 8 \times 8$ in supercell calculations.

In our supercell calculations, we remove one (charge-neutral) oxygen atom in $LiNbO_3$ supercells of different sizes to simulate different oxygen vacancy concentrations. The supercell with oxygen vacancies is charge-neutral, and we fully relax the structure (both lattice constants and internal coordinates) to get the ground-state property.

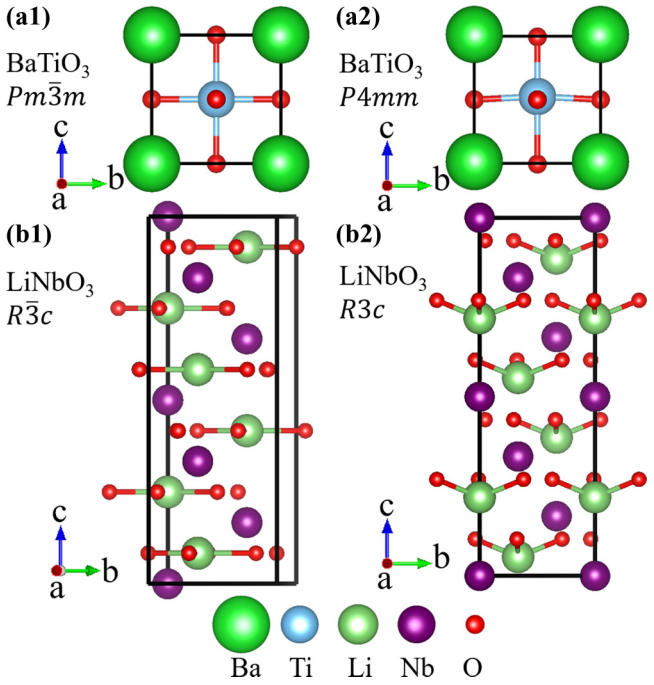

FIG. 1. Atomic structures of $BaTiO_3$ and $LiNbO_3$. Panels (a1) and (a2) show cubic $Pm\bar{3}m$ and tetragonal $P4mm$ structures of $BaTiO_3$, respectively. Panels (b1) and (b2) show centrosymmetric $R\bar{3}c$ and noncentrosymmetric $R3c$ structures of $LiNbO_3$, respectively.

We check a higher-energy cutoff (750 eV) and a denser k-point sampling, and we do not find any significant changes in the key results.

III. RESULTS AND DISCUSSION

A. Rigid-band calculations

In the rigid-band approximation, materials are pristine and extra electrons are added to the system with the same amount of uniform positive charges in the background. Figure 1 shows the crystal structures of pristine $BaTiO_3$ and $LiNbO_3$, which are used in rigid-band modeling. Panels (a1) and (a2) show the crystal structure of cubic $BaTiO_3$ (space group $Pm\bar{3}m$) and tetragonal $BaTiO_3$ (space group $P4mm$). Insulating ferroelectrics have a spontaneous polarization [45]. However, in doped ferroelectrics, partially filled bands may lead to conduction, and polarization becomes ill-defined [46–48]. Therefore, we use cation displacements to characterize the extent of being "polar." In n-doped $BaTiO_3$, we calculate both Ba-O and Ti-O cation displacements along the c-axis, denoted by $\delta_{\text{Ba-O}}$ and $\delta_{\text{Ti-O}}$, as a function of electron concentration. $\delta_{\text{Ba-O}}$ and $\delta_{\text{Ti-O}}$ are explicitly shown in Fig. S1 in the Supplemental Material [49]. Panels (b1) and (b2) show the crystal structure of centrosymmetric $LiNbO_3$ (space group $R\bar{3}c$) and noncentrosymmetric $LiNbO_3$ (space group $R3c$). We calculate both Li-O and Nb-O displacements $\delta_{\text{Li-O}}$ and $\delta_{\text{Nb-O}}$. In the centrosymmetric structure $R\bar{3}c$, each Li atom is surrounded by three oxygen atoms, and all four atoms form a plane that is perpendicular to the c-axis. In the noncentrosymmetric structure $R3c$, the three oxygen atoms still form a plane that is perpendicular to the c-axis but the Li atom deviates from

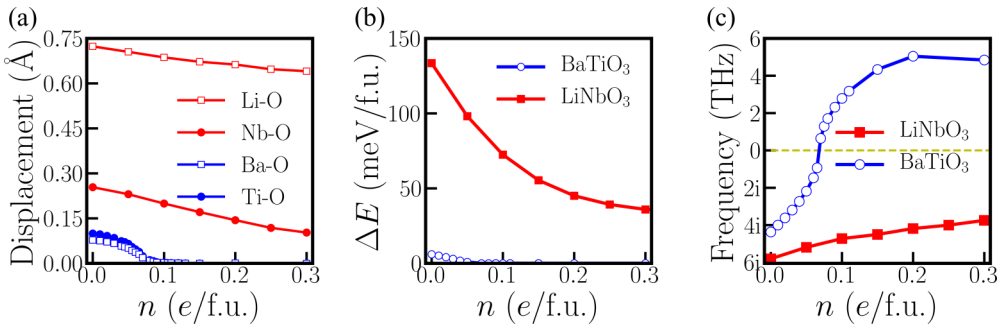

FIG. 2. (a) Ba-O, Ti-O, Li-O, and Nb-O displacements in noncentrosymmetric structures of $BaTiO_3$ and $LiNbO_3$ as a function of electron doping. (b) Energy difference between the centrosymmetric and the noncentrosymmetric structures of $BaTiO_3$ and $LiNbO_3$ as a function of electron doping. (c) Phonon frequency of the zone-center ferroelectric mode of cubic $BaTiO_3$ and $R\bar{3}c$ $LiNbO_3$ as a function of electron doping.

that plane. The distance between the Li atom and the plane that the three oxygen atoms form is defined as the Li-O displacement $\delta_{\text{Li-O}}$. In the centrosymmetric structure $R\bar{3}c$, each Nb atom is at the center of an NbO_6 oxygen octahedron. In the noncentrosymmetric structure $R3c$, Nb atoms move off the center of the NbO_6 oxygen octahedron. The distance between the Nb position and the center of the oxygen octahedron in the $R3c$ structure is defined as $\delta_{\text{Nb-O}}$. $\delta_{\text{Li-O}}$ and $\delta_{\text{Nb-O}}$ are explicitly shown in Fig. S2 in the Supplemental Material [49].

Figure 2 summarizes the key results from rigid-band calculations. Panel (a) shows the cation displacements of tetragonal $BaTiO_3$ (space group $P4mm$) and noncentrosymmetric $LiNbO_3$ (space group $R3c$). In the undoped case, $\delta_{\text{Ba-O}} = 0.077$ Å and $\delta_{\text{Ti-O}} = 0.099$ Å in $BaTiO_3$, and $\delta_{\text{Li-O}} = 0.723$ Å and $\delta_{\text{Nb-O}} = 0.261$ Å in $LiNbO_3$, both of which are in good agreement with previous calculations and experiments [7,50–52]. Upon doping, all of the cation displacements decrease with increasing electron concentration. $\delta_{\text{Ba-O}}$ and $\delta_{\text{Ti-O}}$ in n-doped $BaTiO_3$ vanish at $n_c \simeq 0.1$ e/f.u., which is consistent with previous calculations [26]. However, $\delta_{\text{Li-O}}$ and $\delta_{\text{Nb-O}}$ in n-doped $LiNbO_3$ persist up to 0.3 e/f.u. Furthermore, in n-doped $BaTiO_3$, $\delta_{\text{Ba-O}}$ and $\delta_{\text{Ti-O}}$ decay at approximately the same rate. But in n-doped $LiNbO_3$, $\delta_{\text{Li-O}}$ decays more slowly than $\delta_{\text{Nb-O}}$. With 0.3 e/f.u. electron doping, Nb-O displacements are reduced by about 50% from the undoped value, while Li-O displacements are reduced by only about 10%. This indicates that the off-center movements of Li atoms are very robust and more persistent than Nb-O displacements in a metallic environment. This helps to create an approximate polar metallic phase when $LiNbO_3$ is electron-doped.

Panel (b) of Fig. 2 shows the energy difference between the centrosymmetric structure and the noncentrosymmetric structure of $BaTiO_3$ and $LiNbO_3$. Specifically, for $BaTiO_3$, $\Delta E = E(Pm\bar{3}m) - E(P4mm)$ and for $LiNbO_3$, $\Delta E = E(R\bar{3}c) - E(R3c)$. $\Delta E > 0$ indicates that the noncentrosymmetric structure is favored. In the undoped case, the noncentrosymmetric structure is favored in both $BaTiO_3$ and $LiNbO_3$, i.e., they are both ferroelectric. Upon doping, $BaTiO_3$ is polar until $n_c \simeq 0.1e$/f.u., consistent with the critical concentration found for $\delta_{\text{Ba-O}}$ and $\delta_{\text{Ti-O}}$. For n-doped $LiNbO_3$, ΔE quickly decreases but it stays positive (up to 0.3 e/f.u.). This is consistent with $\delta_{\text{Li-O}}$ and $\delta_{\text{Nb-O}}$, which do not vanish with electron doping (up to 0.3 e/f.u.).

Panel (c) of Fig. 2 shows the zone-center phonon frequency of the ferroelectric mode for centrosymmetric $BaTiO_3$ (space group $Pm\bar{3}m$) and $LiNbO_3$ (space group $R\bar{3}c$). For cubic $Pm\bar{3}m$ $BaTiO_3$, the ferroelectric mode has imaginary phonon frequency with small electron doping, indicating ferroelectric instability. Around the critical doping of $n_c \simeq 0.1$ e/f.u., the phonon frequency of the ferroelectric mode becomes positive and the cubic structure is stabilized. For centrosymmetric $R\bar{3}c$ $LiNbO_3$, the ferroelectric mode always has imaginary phonon frequency (up to 0.3 e/f.u.), indicating that ferroelectric instability persists in n-doped $LiNbO_3$. For both materials, the phonon property of the centrosymmetric structures is consistent with the results of the noncentrosymmetric structures shown in panels (a) and (b). We note that the magnitude of the imaginary phonon mode indicates how unstable the high-symmetry structure is subject to a collective atomic distortion. However, the energy difference between the distorted and undistorted crystal structures reflects not only the instability of the high-symmetry structure, but also other factors. From our calculations, we find that for $BaTiO_3$, the volume of its undistorted structure is 0.5% smaller than that of the distorted structure; in contrast, for $LiNbO_3$, the volume of its undistorted structure is 1.5% larger than that of the distorted structure. The elastic energy change from the high-symmetry structure to the low-symmetry structure is very different between $BaTiO_3$ and $LiNbO_3$. This information is embodied in the total energy difference but is not directly reflected in the imaginary phonon modes.

We also use the PBEsol functional to check the key results in Fig. 2, and we do not find significant changes (see Fig. S4 in the Supplemental Material [49]). Our finding that polar displacements of $LiNbO_3$ are persistent in the presence of conduction electrons is related to the fact that $LiNbO_3$ is hyperferroelectric [53,54], i.e., a ferroelectric material whose polarization does not get suppressed by depolarization fields. This implies that doping a hyperferroelectric material is a viable approach to generating an approximate polar metallic phase.

Next, we study the electronic structure and screening length obtained from rigid-band calculations. Panels (a1) and (a2) of Fig. 3 show the density of states of undoped and doped $BaTiO_3$ (with 0.2 e/f.u. doping). With electron doping, the Fermi level is shifted from the band gap into Ti d states. Panels (b1) and (b2) of Fig. 3 show the density of states of undoped

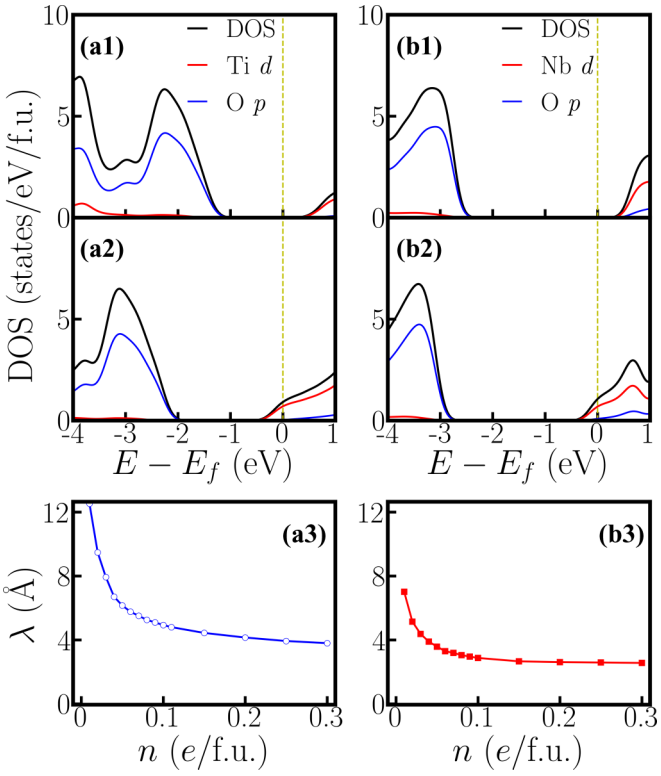

FIG. 3. (a1) Density of states of undoped $BaTiO_3$. (a2) Density of states of doped $BaTiO_3$ with 0.2 e/f.u. doping. The black, red, and blue are total, Ti d, and O p projected densities of states, respectively. (b1) Density of states of undoped $LiNbO_3$. (b2) Density of states of doped $LiNbO_3$ with 0.2 e/f.u. doping. The black, red, and blue are total, Nb d, and O p projected densities of states, respectively. (a3) Thomas-Fermi screening length λ of doped $BaTiO_3$ as a function of electron doping n. (b3) Thomas-Fermi screening length λ of doped $LiNbO_3$ as a function of electron doping n.

and doped $LiNbO_3$ (with 0.2 e/f.u. doping). Similarly, with electron doping, the Fermi level is shifted from the band gap into Nb d states. With the density of states of n-doped $BaTiO_3$ and n-doped $LiNbO_3$, we can estimate the screening length λ by using the Thomas-Fermi model [26]:

$$\lambda = \sqrt{\frac{\epsilon}{e^2 \times D(E_f)}}, \tag{1}$$

where ϵ is the dielectric constant of undoped materials and $D(E_f)$ is the density of states at the Fermi level. For dielectric constants, we use experimental values $\epsilon \approx 44\epsilon_0$ for $BaTiO_3$ [55] and $\epsilon \approx 24\epsilon_0$ for $LiNbO_3$ [56]. Panel (c) of Fig. 3 shows the screening length of n-doped $BaTiO_3$ and n-doped $LiNbO_3$. We find that for both materials upon electron doping, the screening length is on the order of a few Å. Given an electron concentration, n-doped $LiNbO_3$ even has a screening length slightly smaller than n-doped $BaTiO_3$, implying a stronger screening property. The stronger screening property of electron-doped $LiNbO_3$ is due to the fact that undoped $LiNbO_3$ has a smaller dielectric constant than that of $BaTiO_3$, while the density of states at the Fermi level plays a minor role [the ratio of $D(E_f)_{LiNbO_3}$ to $D(E_f)_{BaTiO_3}$ ranges from 0.9 to 1.1 as n changes from 0 to 0.3 e/f.u.].

B. Supercell calculations

Our rigid-band calculations show that polar displacements and conduction can coexist in both n-doped $BaTiO_3$ and n-doped $LiNbO_3$, but the overall polar property (magnitude of polar displacements, polar instability, etc.) is much more enhanced in n-doped $LiNbO_3$ than in n-doped $BaTiO_3$. However, rigid-band calculations do not specify the origin of electron doping, and also they imply that all carriers are uniformly distributed. In real experiments, oxygen vacancies are commonly seen in complex oxides, and each oxygen vacancy nominally donates two electrons. However, an isolated oxygen vacancy may form a defect state, which can localize conduction electrons [57,58]. Some experiments show that in oxygen-reduced $BaTiO_{3-\delta}$, phase separation occurs. Cation displacements $\delta_{\text{Ti-O}}$ only occur in the insulating region and vanish in the metallic region. The overall sample may be considered as a mixture of two different phases [22]. To test whether the results from the rigid-band calculations remain valid in real materials, we perform supercell calculations and consider charge-neutral oxygen vacancies as the electron doping source. We use a 119-atom cell of $BaTiO_{3-\delta}$ and $LiNbO_{3-\delta}$. In both cases, the oxygen vacancy concentration is 4.2%/f.u. A charge-neutral oxygen vacancy donates two electrons to the system, therefore it is an electron doping of 0.084 e/f.u. ($\simeq 1.5 \times 10^{21}$ cm^{-3}), close to the critical doping in n-doped $BaTiO_3$ obtained from rigid-band calculations.

Figure 4(a1) shows the crystal structure of a 119-atom $BaTiO_{3-\delta}$ supercell that contains one oxygen vacancy. For clarity, Ba atoms are not explicitly shown and the oxygen vacancy is highlighted by the orange open circle. Figure 4(a2) shows the cation displacement $\delta_{\text{Ti-O}}$ for each Ti atom in the $BaTiO_{3-\delta}$ supercell (the definition of $\delta_{\text{Ti-O}}$ is identical to that in the rigid-band calculations). Displacements along the c-axis of each Ba atom are explicitly shown in Fig. S3 in the Supplemental Material [49]. We find that while there is some small variation in $\delta_{\text{Ti-O}}$ due to an inhomogeneous chemical environment, $\delta_{\text{Ti-O}}$ on average is reduced to zero. For comparison, we also show the $\delta_{\text{Ti-O}}$ in pristine $BaTiO_3$ in panel (a2), and the suppression of polar displacements by electron doping is evident. Figure 4(a3) shows an isovalue surface of conduction electron density in oxygen-reduced $BaTiO_{3-\delta}$ with $\delta = 4.2\%$. Conduction electrons reside on Ti atoms. Because the polar displacements are suppressed and the material is close to a cubic structure, conduction electrons occupy three Ti t_{2g} orbitals with approximately equal occupancy. This leads to an isovalue surface of a dicelike shape. Figure 4(a4) shows the number of conduction electrons on each Ti atom by integrating the Ti d states from the band gap to the Fermi level. We find that in the presence of oxygen vacancy, while there is non-negligible variation in conduction electron distribution, insulating-metallic phase separation does not occur in our first-principles calculations. Each Ti atom in the supercell has a sizable amount of conduction electron. The results of oxygen-reduced $BaTiO_{3-\delta}$ from supercell calculations are very consistent with rigid-band calculations. We also use the LDA + U method and change the supercell size to test the robustness of this conclusion (see the Supplemental Material for details [49]). We find that in oxygen-reduced $BaTiO_{3-\delta}$, conduction electrons on each Ti atom are almost uniformly distributed.

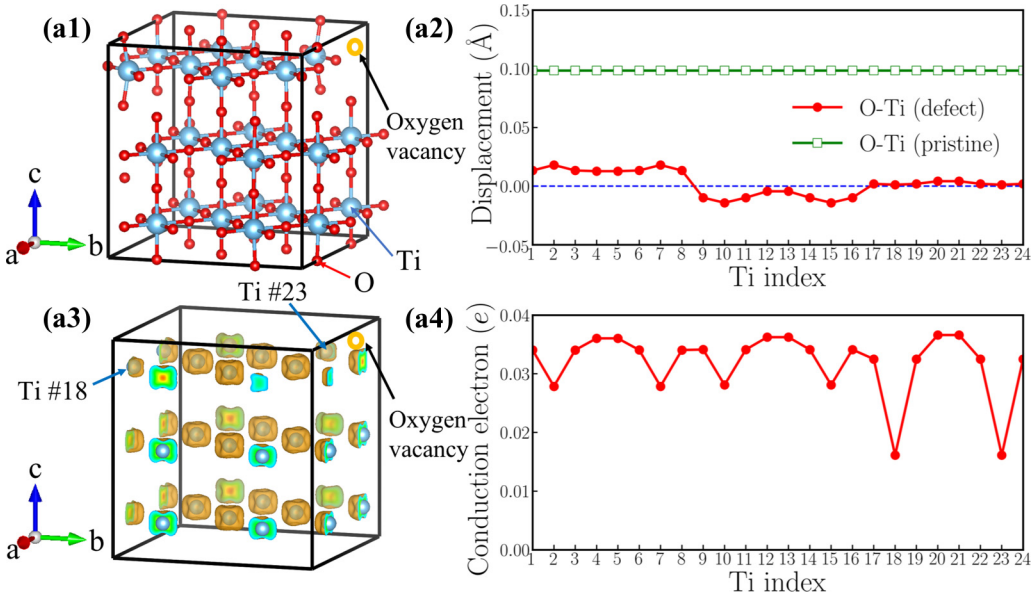

FIG. 4. (a1) Atomic structure of a 119-atom $BaTiO_{3-\delta}$ supercell that contains an oxygen vacancy. For clarity, Ba atoms are not shown. The blue and red balls represent Ti and O atoms. (a2) Polar displacements of each Ti atom. The red circles are calculated from the 119-atom cell. The green squares are bulk $\delta_{\text{Ti-O}}$ of pristine $BaTiO_3$. (a3) An isovalue surface of conduction electron distribution in oxygen-reduced $BaTiO_{3-\delta}$ with $\delta = 4.2\%$. The two nearest-neighbor Ti atoms are highlighted. (a4) Conduction electrons on each Ti atom in the 119-atom cell (the number of conduction electrons on each Ti atom is obtained by integrating Ti d states from the band gap to the Fermi level).

However, supercell calculations of oxygen-reduced $LiNbO_{3-\delta}$ show more complicated results than rigid-band calculations. Figure 5(a1) shows the crystal structure of a 119-atom $LiNbO_3$ supercell that contains one oxygen vacancy. The oxygen vacancy is highlighted by the orange open circle. Figure 5(a2) shows $\delta_{\text{Li-O}}$ for each Li atom and $\delta_{\text{Nb-O}}$ for each Nb atom in the $LiNbO_{3-\delta}$ supercell (the definitions of $\delta_{\text{Li-O}}$ and $\delta_{\text{Nb-O}}$ are identical to those in the rigid-band calculations). We find that while there is non-negligible variation in $\delta_{\text{Li-O}}$ and $\delta_{\text{Nb-O}}$, the cation displacements on each Li and Nb atoms are nonzero throughout the supercell. For comparison, we also show

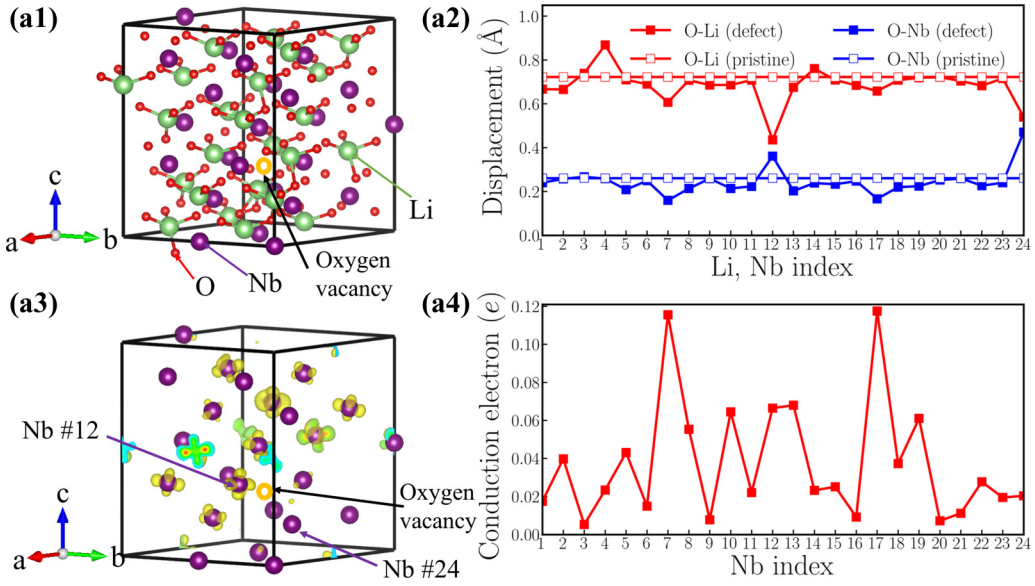

FIG. 5. (a1) Atomic structure of a 119-atom $LiNbO_3$ supercell that contains an oxygen vacancy. The green, purple, and red balls represent Li, Nb, and O atoms, respectively. The orange circle highlights an oxygen vacancy. (a2) Polar displacements of each Li (red square) and Nb atom (blue square). The solid squares are calculated from the 119-atom cell. The open squares are bulk $\delta_{\text{Li-O}}$ and $\delta_{\text{Nb-O}}$ of pristine $LiNbO_3$. (a3) An isovalue surface of conduction electron distribution in oxygen-reduced $LiNbO_{3-\delta}$ with $\delta = 4.2\%$. The two nearest-neighbor Nb atoms are highlighted. (a4) Conduction electrons on each Nb atom in the 119-atom cell (the number of conduction electrons on each Nb atom is obtained by integrating Nb d states from the band gap to the Fermi level).

the $\delta_{\text{Li-O}}$ and $\delta_{\text{Nb-O}}$ in pristine $LiNbO_3$ in panel (a2). We find that in the presence of oxygen vacancy in $LiNbO_{3-\delta}$, the cation displacements are still substantial compared to undoped $LiNbO_3$.

The average value of $\delta_{\text{Li-O}}$ is 0.68 Å and the average value of $\delta_{\text{Nb-O}}$ is 0.24 Å, both of which are close to the results of rigid-band calculations with the same electron concentration (in the rigid-band approximation, $\delta_{\text{Li-O}}$ is 0.69 Å and $\delta_{\text{Nb-O}}$ is 0.21 Å). Figure 5(a3) shows an isovalue surface of conduction electron distribution in oxygen-reduced $LiNbO_{3-\delta}$ with $\delta = 4.2\%$. Different from oxygen-reduced $BaTiO_{3-\delta}$, which has almost uniform conduction electron distribution, some of the Nb atoms have negligible conduction electrons, indicating that those Nb sites are almost insulating. This phenomenon can be more clearly seen from Fig. 5(a4), which shows the number of conduction electrons on each Nb site by integrating Nb d states from the band gap to the Fermi level. Nb no. 3, no. 9, and no. 20 have less than 0.01 e per atom, while Nb no. 7 and no. 17 have more than 0.12 e per atom. With electron doping in $LiNbO_3$, the conduction electrons on Nb sites are far from uniformly distributed. This implies that the charge disproportionation of conduction electrons on Nb atoms occurs in real materials. Such charge disproportion can be suppressed with a higher electron concentration. We calculated oxygen-reduced $LiNbO_{3-\delta}$ with $\delta = 8.4\%$. Cation displacements and conduction electron distribution on Nb d states are shown in Fig. S9 in the Supplemental Material [49]. While there is non-negligible variation in the electron distribution, all Nb atoms have conduction electrons with a higher concentration of oxygen vacancies, as expected.

Finally, we estimate the formation energy of a charge-neutral oxygen vacancy in $BaTiO_{3-\delta}$ and in $LiNbO_{3-\delta}$ using a supercell calculation. We study a charge-neutral oxygen vacancy by removing an oxygen atom from a charge-neutral supercell. The definition of formation energy of a charge-neutral oxygen vacancy in the oxygen-rich limit is

$$\Delta E_{\text{O}}^{f} = E_T(V_{\text{O}}) - E_{T0} + \tfrac{1}{2}E_{\text{O}_2}, \tag{2}$$

where $E_T(V_{\text{O}})$ is the total energy of a supercell with one oxygen vacancy, and E_{T0} is the total energy of a pristine supercell. E_{O_2} is the total energy of an oxygen molecule (obtained in a spin-polarized calculation).

Figure 6 shows the oxygen vacancy formation energy in oxygen-reduced $BaTiO_{3-\delta}$ and oxygen-reduced $LiNbO_{3-\delta}$ as a function of oxygen vacancy concentration. Red points and blue triangles are the formation energies of oxygen vacancy in $BaTiO_{3-\delta}$ and $LiNbO_{3-\delta}$, respectively. The blue cross is a reference value from previous works [59].

We use different supercells to test different concentrations of oxygen vacancies. The formation energy of an oxygen vacancy does not have a strong dependence on vacancy concentration, implying that the vacancy concentration is low enough such that vacancy-vacancy interaction is negligible. The formation energy of a charge-neutral oxygen vacancy in $LiNbO_{3-\delta}$ is larger than that in $BaTiO_{3-\delta}$ by about 0.9 eV per vacancy. This is reasonable considering the fact that the gap of $LiNbO_3$ is larger than that of $BaTiO_3$ by about 1 eV (see Fig. 3). While the formation energy of oxygen vacancy in $LiNbO_{3-\delta}$ is higher, oxygen vacancy has been widely observed in $LiNbO_{3-\delta}$ in experiments [60–63].

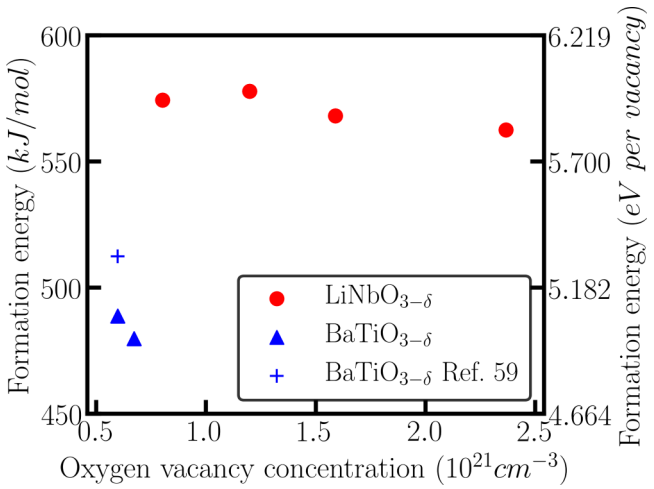

FIG. 6. Oxygen vacancy formation energy in oxygen-reduced $BaTiO_{3-\delta}$ (blue triangles) and in oxygen-reduced $LiNbO_{3-\delta}$ (red circles) as a function of oxygen vacancy concentration. The blue cross is a reference value from previous works [59].

IV. CONCLUSION

In conclusion, we perform first-principles calculations to study the possible coexistence of conduction electrons and polar distortions in n-doped $BaTiO_3$ and n-doped $LiNbO_3$, using both rigid-band modeling and more realistic supercell calculations. From rigid-band modeling, we find that upon electron doping, cation displacements in $BaTiO_3$ are quickly reduced and completely vanish at a critical electron concentration of 0.1 e/f.u. In contrast, in n-doped $LiNbO_3$, Li-O and Nb-O displacements are significantly larger than cation displacements in n-doped $BaTiO_3$, and more importantly they are much more robust and can persist even at a concentration of 0.3 e/f.u. In n-doped $LiNbO_3$, Li-O displacements decay more slowly than Nb-O displacements, while in n-doped $BaTiO_3$, Ba-O and Ti-O displacements decay approximately at the same rate. From supercell calculations (using oxygen vacancy as electron donors), we find that in $BaTiO_{3-\delta}$ with $\delta = 4.2\%$, cation displacements in $BaTiO_3$ are almost completely suppressed, which is consistent with the result of rigid-band modeling. Conduction electrons on Ti atoms are uniformly distributed, underlying rigid-band calculations. On the other hand, the results of oxygen-reduced $LiNbO_{3-\delta}$ ($\delta = 4.2\%$) from supercell calculations are more complicated than rigid-band calculations. Substantial polar displacements $\delta_{\text{Li-O}}$ and $\delta_{\text{Nb-O}}$ occur throughout the supercell, but strong variations are found in conduction electron distribution. This implies that the rigid-band approximation should be used with caution in simulating electron-doped $LiNbO_3$ and related oxides.

Our work indicates that electron doping of $LiNbO_3$-type ferroelectrics is a simple and feasible approach to approximately creating the rare polar metallic phase. Incorporating doped ferroelectric semiconductors (in particular $LiNbO_3$-type ferroelectrics) into devices may lead to new functionality and applications.

ACKNOWLEDGMENTS

H.C. is supported by the National Natural Science Foundation of China under Project No. 11774236, Shanghai Pujiang Talents Program (Grant No. 17PJ1407300) and Seed grant of NYU-ECNU Research Institute of Physics. Y.C. and C.X. are supported by Research Grants Council of Hong Kong under Projects No. 17200017 and No. 17300018, and the National Natural Science Foundation of China under Project No. 11874313. NYU Shanghai HPC and HKU-ITS provided computational resources.

[1] D. Puggioni and J. M. Rondinelli, Nat. Commun. **5**, 3432 (2014).

[2] Y. Cao, Z. Wang, S. Y. Park, Y. Yuan, X. Liu, S. M. Nikitin, H. Akamatsu, M. Kareev, S. Middey, D. Meyers *et al.*, Nat. Commun. **9**, 1547 (2018).

[3] P. V. Balachandran, J. Young, T. Lookman, and J. M. Rondinelli, Nat. Commun. **8**, 14282 (2017).

[4] K. Page, T. Kolodiazhnyi, T. Proffen, A. K. Cheetham, and R. Seshadri, Phys. Rev. Lett. **101**, 205502 (2008).

[5] J. A. Bock, S. Lee, S. Trolier-McKinstry, and C. A. Randall, Appl. Phys. Lett. **107**, 092902 (2015).

[6] L. S. McCarty and G. M. Whitesides, Angew. Chem., Int. Ed. **47**, 2188 (2008).

[7] K. M. Rabe, C. H. Ahn, and J.-M. Triscone, *Physics of Ferroelectrics: A Modern Perspective* (Springer Science & Business Media, Berlin, 2007), Vol. 105.

[8] A. Mooradian and G. Wright, Phys. Rev. Lett. **16**, 999 (1966).

[9] J. Bowlan, Ph.D. thesis, Georgia Institute of Technology (2010).

[10] N. A. Hill, J. Phys. Chem. B **104**, 6694 (2000).

[11] P. W. Anderson and E. Blount, Phys. Rev. Lett. **14**, 217 (1965).

[12] Y. Shi, Y. Guo, X. Wang, A. J. Princep, D. Khalyavin, P. Manuel, Y. Michiue, A. Sato, K. Tsuda, S. Yu *et al.*, Nat. Mater. **12**, 1024 (2013).

[13] H. Xiang, Phys. Rev. B **90**, 094108 (2014).

[14] G. Giovannetti and M. Capone, Phys. Rev. B **90**, 195113 (2014).

[15] H. M. Liu, Y. P. Du, Y. L. Xie, J. M. Liu, C. G. Duan, and X. Wan, Phys. Rev. B **91**, 064104 (2015).

[16] E. I. P. Aulesti, Y. W. Cheung, Y.-W. Fang, J. He, K. Yamaura, K. T. Lai, S. K. Goh, and H. Chen, Appl. Phys. Lett. **113**, 012902 (2018).

[17] I. Lo Vecchio, G. Giovannetti, M. Autore, P. Di Pietro, A. Perucchi, J. He, K. Yamaura, M. Capone, and S. Lupi, Phys. Rev. B **93**, 161113(R) (2016).

[18] H. Sim and B. G. Kim, Phys. Rev. B **89**, 201107(R) (2014).

[19] H. Padmanabhan, Y. Park, D. Puggioni, Y. Yuan, Y. Cao, L. Gasparov, Y. Shi, J. Chakhalian, J. M. Rondinelli, and V. Gopalan, Appl. Phys. Lett. **113**, 122906 (2018).

[20] Z. Fei, W. Zhao, T. A. Palomaki, B. Sun, M. K. Miller, Z. Zhao, J. Yan, X. Xu, and D. H. Cobden, Nature (London) **560**, 336 (2018).

[21] T. Kim, D. Puggioni, Y. Yuan, L. Xie, H. Zhou, N. Campbell, P. Ryan, Y. Choi, J.-W. Kim, J. Patzner *et al.*, Nature (London) **533**, 68 (2016).

[22] I.-K. Jeong, S. Lee, S.-Y. Jeong, C. J. Won, N. Hur, and A. Llobet, Phys. Rev. B **84**, 064125 (2011).

[23] J. Hwang, T. Kolodiazhnyi, J. Yang, and M. Couillard, Phys. Rev. B **82**, 214109 (2010).

[24] T. Kolodiazhnyi, M. Tachibana, H. Kawaji, J. Hwang, and E. Takayama-Muromachi, Phys. Rev. Lett. **104**, 147602 (2010).

[25] T. Kolodiazhnyi, Phys. Rev. B **78**, 045107 (2008).

[26] Y. Wang, X. Liu, J. D. Burton, S. S. Jaswal, and E. Y. Tsymbal, Phys. Rev. Lett. **109**, 247601 (2012).

[27] S. Raghavan, J. Y. Zhang, O. F. Shoron, and S. Stemmer, Phys. Rev. Lett. **117**, 037602 (2016).

[28] C. Won, Y. Park, K. Lee, H. Ryu, and N. Hur, J. Appl. Phys. **109**, 084108 (2011).

[29] D. Bohm and D. Pines, Phys. Rev. **92**, 609 (1953).

[30] W. Cochran, Adv. Phys. **9**, 387 (1960).

[31] V. M. Galitski and S. Das Sarma, Phys. Rev. B **70**, 035111 (2004).

[32] Q. Zhang, T. Cagin, and W. A. Goddard, Proc. Natl. Acad. Sci. USA **103**, 14695 (2006).

[33] R. E. Cohen, Nature (London) **358**, 136 (1992).

[34] Y. Furukawa, K. Kitamura, A. Alexandrovski, R. Route, M. Fejer, and G. Foulon, Appl. Phys. Lett. **78**, 1970 (2001).

[35] G. Nataf, P. Grysan, M. Guennou, J. Kreisel, D. Martinotti, C. Rountree, C. Mathieu, and N. Barrett, Sci. Rep. **6**, 33098 (2016).

[36] K. Nakamura, J. Kurz, K. Parameswaran, and M. Fejer, J. Appl. Phys. **91**, 4528 (2002).

[37] Y. Noguchi, R. Inoue, and M. Miyayama, Adv. Condens. Matter Phys. **2016**, 2943173 (2016).

[38] P. Hohenberg and W. Kohn, Phys. Rev. **136**, B864 (1964).

[39] W. Kohn and L. J. Sham, Phys. Rev. **140**, A1133 (1965).

[40] M. C. Payne, M. P. Teter, D. C. Allan, T. Arias, and A. J. Joannopoulos, Rev. Mod. Phys. **64**, 1045 (1992).

[41] G. Kresse and J. Furthmüller, Phys. Rev. B **54**, 11169 (1996).

[42] D. M. Ceperley and B. J. Alder, Phys. Rev. Lett. **45**, 566 (1980).

[43] J. P. Perdew, A. Ruzsinszky, G. I. Csonka, O. A. Vydrov, G. E. Scuseria, L. A. Constantin, X. Zhou, and K. Burke, Phys. Rev. Lett. **100**, 136406 (2008).

[44] Y. Zhang, J. Sun, J. P. Perdew, and X. Wu, Phys. Rev. B **96**, 035143 (2017).

[45] S. Abrahams, S. Kurtz, and P. Jamieson, Phys. Rev. **172**, 551 (1968).

[46] X.-L. Wang, S. X. Dou, and C. Zhang, NPG Asia Mater. **2**, 31 (2010).

[47] M. Stengel, P. Aguado-Puente, N. A. Spaldin, and J. Junquera, Phys. Rev. B **83**, 235112 (2011).

[48] J. Fujioka, A. Doi, D. Okuyama, D. Morikawa, T. Arima, K. Okada, Y. Kaneko, T. Fukuda, H. Uchiyama, D. Ishikawa *et al.*, Sci. Rep. **5**, 13207 (2015).

[49] See Supplemental Material at http://link.aps.org/supplemental/10.1103/PhysRevMaterials.3.054405 for additional discussions (details of crystal structures, comparison of LDA and PBEsol calculations, comparison of two type electrons in oxygen reduced $BaTiO_{3-\delta}$ and $LiNbO_{3-\delta}$, and some tests of oxygen reduced supercells.).

[50] Landolt-Bornstein Table, edited by K.-H. Hellwege and A. M. Hellwege (Springer, Berlin, 1969).

[51] A. M. Prokhorov and Y. S. Kuz'Minov, *Physics and Chemistry of Crystalline Lithium Niobate* (CRC, Boca Raton, FL, 1990).
[52] H. H. Nahm and C. Park, Appl. Phys. Lett. **78**, 3812 (2001).
[53] K. F. Garrity, K. M. Rabe, and D. Vanderbilt, Phys. Rev. Lett. **112**, 127601 (2014).
[54] P. Li, X. Ren, G.-C. Guo, and L. He, Sci. Rep. **6**, 34085 (2016).
[55] G. Rupprecht and R. Bell, Phys. Rev. **135**, A748 (1964).
[56] A. Mansingh and A. Dhar, J. Phys. D **18**, 2059 (1985).
[57] B. Magyari-Köpe, S. G. Park, H.-D. Lee, and Y. Nishi, J. Mater. Sci. **47**, 7498 (2012).
[58] C. Lin, D. Shin, and A. A. Demkov, J. Appl. Phys. **117**, 225703 (2015).
[59] M. Choi, F. Oba, and I. Tanaka, Appl. Phys. Lett. **98**, 172901 (2011).
[60] Y. Li, W. G. Schmidt, and S. Sanna, Phys. Rev. B **91**, 174106 (2015).
[61] G. G. DeLeo, J. L. Dobson, M. F. Masters, and L. H. Bonjack, Phys. Rev. B **37**, 8394 (1988).
[62] D. Smyth, Ferroelectrics **50**, 93 (1983).
[63] K. Sweeney and L. Halliburton, Appl. Phys. Lett. **43**, 336 (1983).